ADVANCED FUNCTIONAL MATERIALS
www.afm-journal.de

Highly Uniform, Electroforming-Free, and Self-Rectifying Resistive Memory in the Pt/Ta_2O_5/HfO_{2-x}/TiN Structure

*Jung Ho Yoon, Seul Ji Song, Il-Hyuk Yoo, Jun Yeong Seok, Kyung Jean Yoon, Dae Eun Kwon, Tae Hyung Park, and Cheol Seong Hwang**

The development of a resistance switching (RS) memory cell that contains rectification functionality in itself, highly reproducible RS performance, and electroforming-free characteristics is an impending task for the development of resistance switching random access memory. In this work, a two-layered dielectric structure consisting of HfO_2 and Ta_2O_5 layers, which are in contact with the TiN and Pt electrode, is presented for achieving these tasks simultaneously in one sample configuration. The HfO_2 layer works as the resistance switching layer by trapping or detrapping of electronic carriers, whereas the Ta_2O_5 layer remains intact during the whole switching cycle, which provides the rectification. With the optimized structure and operation conditions for the given materials, excellent RS uniformity, electroforming-free, and self-rectifying functionality could be simultaneously achieved from the Pt/Ta_2O_5/HfO_2/TiN structure.

1. Introduction

Resistance switching random access memory (ReRAM) is attracting a great deal of attention as one of the most promising next-generation non-volatile memory devices especially in the crossbar array (CBA) configuration.[1–5] It currently has several obstacles to overcome, however, such as the high variability in electrical performances, the requirement of an electroforming step, and the necessary integration of a memory cell with selector devices to alleviate the sneak currents in CBA.[6] These problems become even more serious when a three-dimensional (vertical) CBA structure is to be fabricated.[6] The former two problems are generally related to the localized (soft) breakdown of the dielectric layers in many metal-insulator-metal (MIM) structures, which is the typical configuration of memory cells in ReRAM or CBA, to induce the formation of conducting filaments (CFs), while the third problem is more closely related with the integration issues of the device in planar and vertical CBA structures. As the electrical resistance switching (RS) in many reported systems is closely related with the formation and (local) rupture of the CFs in the insulator layer of the MIM structure,[7–9] which can usually be initiated by the electroforming step,[10,11] the random fluctuations of RS parameters, such as the voltages for the switching and current levels in the low resistance state (LRS) and high resistance state (HRS), are somewhat inevitable. This must be more obvious for the cases where the CFs show distinctive phase transition from the insulating mother phase, such as the Magnéli CFs in TiO_2.[7,12] In addition, the involvement of the initial electroforming step, which is usually accomplished by adopting a voltage higher than the usual operation voltages, is generally unfavorable for the device fabrication and operation. Therefore, seeking an RS mechanism that does not require an electroforming step, which could also eliminate the involvement of the prominent local CF mechanism, is an important task for the further development of the ReRAM or CBA devices.

The fabrication of selector devices for the random access of the memory cell in their array configuration and integration with the RS memory devices is another crucial task for the successful development of the CBA. The CBA will evolve into the vertically integrated configuration, which does not correspond to the multiple stacking of two-dimensional CBAs.[13] The fabrication of a discrete selector, such as the Schottky diode,[14,15] however, or of highly nonlinear current-voltage (I–V) devices,[16–18] and combining them with the RS memory cell, will be very difficult in the vertically integrated structure.[6] Therefore, the development of an RS memory cell that simultaneously contains rectification functionality in itself (self-rectification), highly reproducible RS performance, and electroforming-free characteristics is an impending task.

HfO_2 is a well-known high-k dielectric material for the advanced field effect transistor,[19] but it also plays a crucial role in the ReRAM field due to its controllability of resistance values in atomic scale.[20,21] Ta_2O_5 is also attracting a high level of interest in the ReRAM field as it has shown an exceptionally high switching endurance, especially when combined with a metastable TaO_x ($x \approx 2$) layer, which serves as the reservoir for the oxygen vacancies (V_o).[5,22] These two materials are characterized as lacking in discrete metallic second phases, as opposed to TiO_2 and WO_3, which are characterized as having

J. H. Yoon, S. J. Song, I.-H. Yoo, J. Y. Seok, K. J. Yoon, D. E. Kwon, T. H. Park, and Prof. C. S. Hwang
Department of Materials Science and Engineering and Inter-university Semiconductor Research Center
Seoul National University, Seoul 151–744
Republic of Korea
E-mail: cheolsh@snu.ac.kr

DOI: 10.1002/adfm.201400064

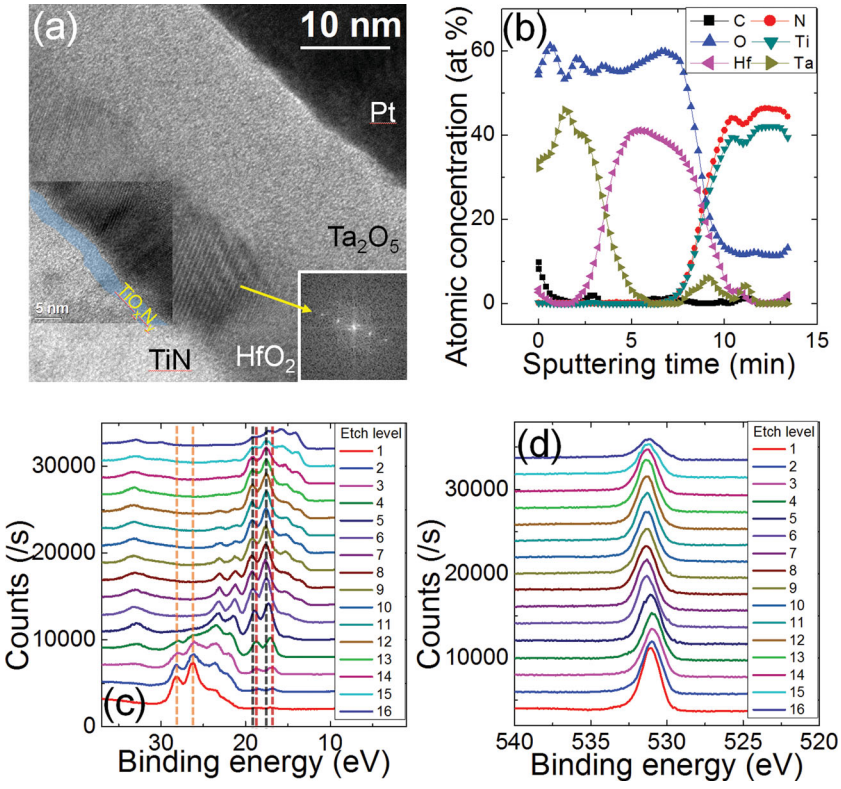

Figure 1. a) Cross-section TEM images and b) depth profiling AES data of the Pt/Ta_2O_5(10nm)/HfO_2(10nm)/TiN sample, and c) Ta *4f*/Hf *4f* and d) O *1s* core levels in the XPS depth profile results of the Ta_2O_5(5nm)/HfO_2(10nm)/TiN sample.

the conducting Magnéli phases (ca. Ti_nO_{2n-1}, n = 3, 4, 5...) in their heavily reduced state.[7,23] Therefore, HfO_2 and Ta_2O_5 could have inherently higher uniformity compared with the other materials mentioned above, but many of the switching reports in these materials still utilized the CF-related mechanism, which is induced by the electroforming at voltages higher than that in the usual switching operations.[5,20–22] In addition, there has been no report on the significantly self-rectifying *I–V* characteristics of these material systems, where the RS is observed in one bias polarity while the current flow in the opposite bias polarity is largely suppressed.

Meanwhile, electronic RS behaviors have been reported in several material systems, which could be mostly attributed to the trapping and detrapping of carriers (mostly electrons) depending on the bias polarities.[24–26] In contrast to other ionic RS mechanisms, which generally involve the movement of (defective) ionic species during the set (switching from HRS to LRS) and reset (switching from LRS to HRS) operations, such electronic switching mechanisms induce no or minimal movement of ionic species, making them inherently immune to the large variations in the switching parameters. It has to be noted that the carriers that discern the LRS and HRS are still electrons or holes, not ions, even in the ionic RS systems. The prerequisites for such electronic RS systems are the presence of a mechanism that can induce the bias-polarity-dependent trapping and detrapping of the electronic carriers, and traps that are deep enough to store the trapped carriers for a sufficiently long time under the repeated read operations at the device operation temperatures. These requirements can be met by the deep traps in the band gap of the switching oxide, whose potential barrier must be asymmetric with respect to the bias polarity or different levels of discrete trap states, which respond differently to the bias depending on the resistance states of the sample.

Presented in this work, therefore, is a material system that can provide a very high uniformity in the switching parameters, which can be obtained without the problematic initial electroforming step, and self-rectifying functionality by combining the two promising dielectric materials, HfO_2 and Ta_2O_5. The key component of the idea is that between the two materials, HfO_2 plays the role of the fluent RS layer without requiring the electroforming step while Ta_2O_5 plays the role of a rectifier with the help of a high-work-function metal, which is the top electrode (TE) Pt in this case. To achieve an electroforming-free and highly uniform RS behavior, the initial defect (V_o) content in the atomic-layer-deposited HfO_2 layer was increased by two means: through the chemical interaction with the TiN bottom electrode (BE) and through the deoxidation effect during the plasma-enhanced atomic layer deposition (PEALD) of the Ta_2O_5 layer on top. Another merit of the present work is that the two functional oxide layers are deposited via ALD (HfO_2) and PEALD (Ta_2O_5), which are the optimal processes for the three-dimensional vertical ReRAM or CBA fabrication. In this structure, the sample with optimized film thicknesses showed highly reliable electronic switching characteristics even at an operation temperature of 85 °C mitigating the concern about the stability of trap-occupied and unoccupied states. This could be ascribed to the deep trap depth in HfO_2 (≈1 eV).

2. Structural Properties of the Ta_2O_5/HfO_2/TiN Thin-Film Stack

The cross-section transmission electron microscopy (TEM) images of the Pt/Ta_2O_5/HfO_2/TiN structure are shown in **Figure 1**a. The figure shows a well-distinguishable layer structure with a crystallized monoclinic HfO_2 layer, confirmed by the fast-Fourier-transformed image (lower right inset) of the crystalline lattice fringes, and an amorphous Ta_2O_5 layer structure. The HfO_2/TiN interface is also clearly defined, but a small amount of amorphous material can be observed at the mostly-grain-boundary regions of the crystalline TiN, which could be the TiO_xN_y material (left inset). There is no evidently oxidized TiO_2 (or TiO_x, x < 2) layer at the interface between HfO_2 and TiN. The well-distinguished $Ta_2O_5/HfO_2/TiO_xN_y$ structure is also confirmed by the depth profiling in Auger electron spectroscopy (AES), as shown in Figure 1b.

The influence of depositing the Ta_2O_5 layer via PEALD on top of the HfO_2 layer can be more evidently understood via X-ray photoelectron spectroscopy (XPS). Figures 1 and d show the Ta *4f*/Hf *4f*, and O *1s* core levels in the XPS depth profile results of the Ta_2O_5(5nm)/HfO_2(10nm)/TiN sample. For the XPS measurement, the Ar^+ ion beam energy was set to 1 keV during the sputter-etching. The core-level data for N *1s* and Ti *2p* were included in the online supplementary information (Figure S1, Supporting Information). The core levels were shown with regard to the etch level, where the time between the levels was ≈10 s. The binding energy of Ta *4f* well coincided with the reported value of the Ta *4f* peak (26.2 eV for Ta $4f_{7/2}$ and 28.1 for Ta $4f_{5/2}$, indicated by the yellow vertical dashed lines in Figure 1c) in Ta_2O_5.[27,28] The emergence of the peaks near the binding energy of ≈22–24 eV was an artifact that originated from the preferential etching of oxygen atoms by the Ar^+ ion bombardment. This suggests that the underlying HfO_2 layer had no significant influence on the chemical properties of the Ta_2O_5 layer. A significant change in the binding energy of Hf *4f* was observed, however, as the XPS probing depth changed from the Ta_2O_5/HfO_2 interface region to the bulk HfO_2 region. The binding energy of the Hf *4f* core levels shifted to a lower binding energy direction near the interface region with the Ta_2O_5 layer (indicated by the brown vertical dashed lines), which recovered the value of the reported Hf *4f* binding energy (17.6 eV for Hf $4f_{5/2}$ and 19.2 for Hf $4f_{3/2}$, indicated by the black vertical dashed lines) of HfO_2[29] as it moved away from the interface. The weak peaks near the binding energy of ~13–15 eV were also due to the preferential etching of oxygen atoms from the HfO_2 layer during the XPS depth profiling. The presence of a lower binding energy peak of Ta *4f* up to the etching level of 13 did not necessarily suggest that Ta_2O_5 was intermixed with HfO_2, but this was believed due to the artifact produced by preferential etching considering the AES profile shown in Figure 1b. This result implies that HfO_{2-x} are formed near the Ta_2O_5 thin-film layer during the PEALD process of the Ta_2O_5 layer. It appears that the impingement effect of ions during the PEALD of the Ta_2O_5 layer induced such defects in the HfO_2 layer. The XPS core levels of O *1s*, N *1s*, and Ti *2p* shown in Figure 1d and online SI Figures S1a and S1b did not show any notable feature, except for the slight shift of the O *1s* peak position to the high-binding-energy direction as the layer changed from Ta_2O_5 to HfO_2. The slight bump near binding energy ~404 eV in the N *1s* spectra was due to the Ta *4p* core level. The presence of O *1s* at etching level >14, which corresponds to mainly TiN, confirmed that the TiN BE was partly oxidized, as shown in Figure 1a. The precise coincidence between the emergences of the Ti and N peaks suggested that the interface between HfO_2 and TiN BE could be quite abrupt, which was consistent with the TEM results shown in Figure 1a. These results suggested that depositing the PEALD Ta_2O_5 layer on top of ALD HfO_2 induced a deoxidizing effect on the HfO_2 layer while the Ta_2O_5 layer itself had a low defect concentration. The application of plasma power during the Ta_2O_5 deposition appeared to impose such deoxidizing effect on the underlying HfO_2 layer. This effect was well represented by the electrical performances of the single and stacked dielectric-layer samples described in the following section.

3. Electrical Performances of the Memory Cell and Switching Mechanism

Figures 2a–d show the RS *I–V* curves of the Pt/10-nm-thick HfO_2/TiN, Pt/5-nm-thick Ta_2O_5/10-nm-thick HfO_2/TiN, Pt/10-nm-thick Ta_2O_5/5-nm-thick HfO_2/TiN, and Pt/10-nm-thick Ta_2O_5/10-nm-thick HfO_2/TiN samples, respectively. The inset figures in Figures 2 and b show the schematic diagrams of the samples with single and stacked dielectric layers. For these I-V tests, Pt TE was biased while TiN BE was grounded, and the compliance current (I_{cc}) was set at between 10 and 100 μA to prevent not only the complete breakdown of the sample but also the emergence of the usual bipolar type switching. The usual bipolar-type switching characteristics are shown in Figure 2e. Briefly, it required electroforming in the negative bias voltage region with the typical electroforming voltage and the current levels of ca. –10 V and 1 μA. This corresponds to ionic switching where the high Schottky barrier at the Pt/HfO_2 or Pt/Ta_2O_5 is locally disrupted and recovered by the drifting movement of the oxygen ions while the oxide/TiN interface maintained (quasi-) Ohmic contact. In contrast, such usual ionic RS mechanism was strictly prohibited in this work by adopting set and reset switching in positive and negative bias polarities, respectively, while the minimum (maximum absolute) voltages in the negative bias region was controlled so as not to induce a large leakage current in that bias region. All the samples showed high resistance in the pristine state, as can be seen from the first set of *I–V* curves (black lines). Among these samples, the Pt/10-nm-thick Ta_2O_5/10-nm-thick HfO_2/TiN sample (Figure 2d) shows a highly desirable RS performance, as will be discussed in detail later. Three notable features could be found in Figure 2. First, the single HfO_2 layer did not show feasible RS behavior (Figure 2a). This sample generally shows an asymmetric *I–V* shape, where the much more fluent electron injection at the HfO_2/TiN interface under the positive bias compared with the suppressed electron injection at the Pt/HfO_2 interface under the negative bias is the reason for the asymmetry. Second, the stacked dielectric layer shows desirable RS curves in the positive bias region when the HfO_2 layer thickness was 10 nm while the current in the negative bias region was generally very low in a wide voltage range irrespective of the resistance state of the samples. Third, a large-enough and clearly distinguishable resistance ratio between the HRS and LRS could have been achieved only when both the HfO_2 and Ta_2O_5 layers were 10-nm-thick (Figure 2d). These three findings suggest that any change in the sample that induced the RS was confined within the HfO_2 layer while the high Schottky barrier at the Pt/Ta_2O_5 interface remained intact during all the switching cycles. Based on the I-V characteristics shown in Figure 2, the Pt/10-nm-thick Ta_2O_5/10-nm-thick HfO_2/TiN sample was chosen, and its detailed RS performances were examined. The general switching sequences are shown by the numbers included in Figure 2d: the *I–V* curves of the pristine state (curve 1, open square symbol); the LRS (curve 2, red line), which was induced by the first voltage sweep up to +12 V with an I_{cc} of 10 μA; the resetting curve (curve 3, blue line), where the voltage was swept down to –10 V; the HRS (curve 4, green line), which was induced by the previous voltage sweep into the negative voltage direction; and the setting curve (curve 5,

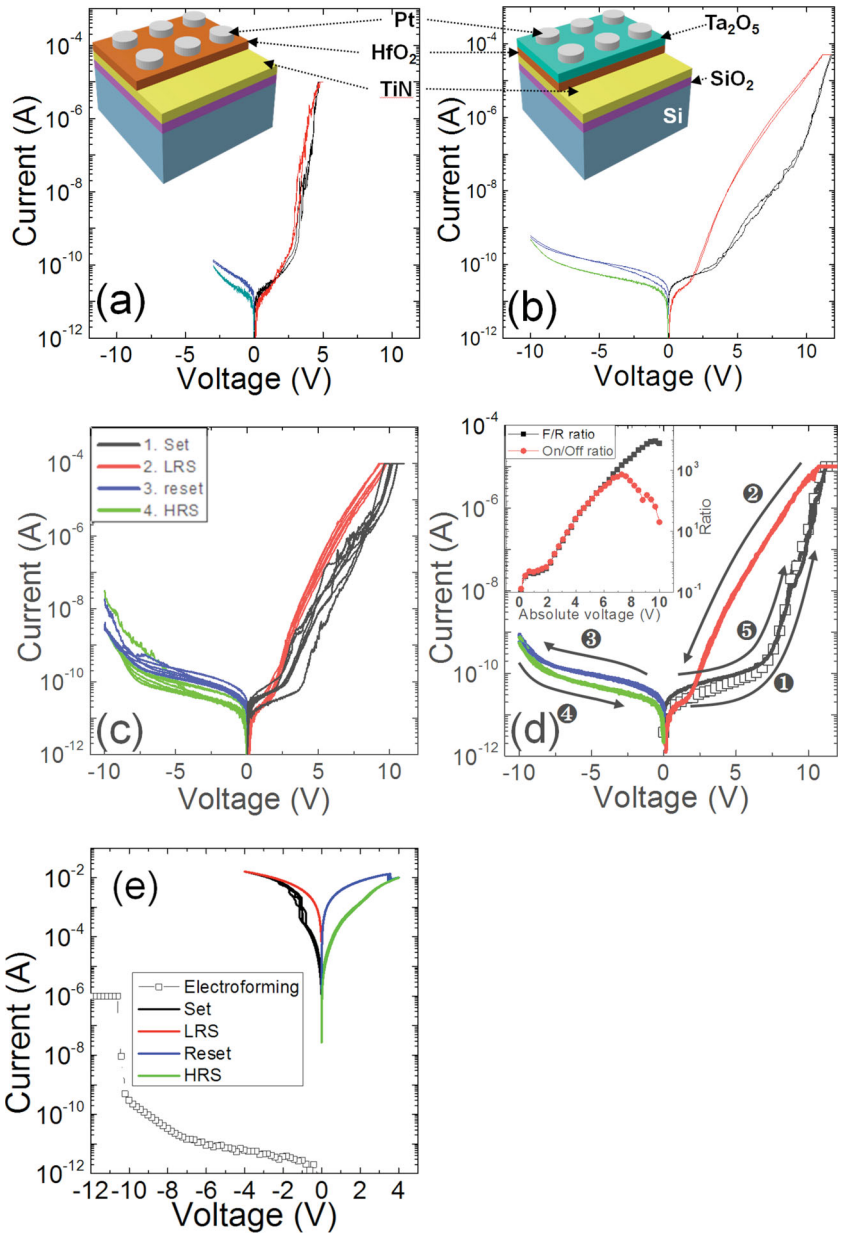

Figure 2. Resistive switching *I–V* curves of the a) Pt/10-nm-thick HfO_2/TiN, b) Pt/5-nm-thick Ta_2O_5/10-nm-thick HfO_2/TiN, c) Pt/10-nm-thick Ta_2O_5/5-nm-thick HfO_2/TiN, and d) Pt/10-nm-thick Ta_2O_5/10-nm-thick HfO_2/TiN samples. Schematic diagrams of the samples with (inset figure of (a)) single and (inset figure of (b)) stacked dielectric layers. (inset figure of (d)) Resistance ratio between HRS and LRS, and rectification ratio (current ratio between the positive (LRS) and negative voltages) as a function of absolute voltage. e) The conventional bipolar resistive switching behavior in the Pt/Ta_2O_5(10nm)/HfO_2(10 nm)/TiN sample. The electroforming was initially performed in the negative bias voltage region with the typical electroforming voltage and the current levels of ca. –10 V and 1 μA. This was not the desired switching operation in this work.

black line) in the positive voltage region, which set the sample to the LRS again. The almost identical shapes of curves 1 and 5 reveal that this was the electroforming-free sample. The resistance ratio between HRS and LRS and the rectification ratio (the current ratio between the positive (LRS) and negative voltages) as a function of absolute voltage was included in the inset figure in Figure 2d. A maximum resistance ratio of ≈10^3 and a rectification ratio of ≈10^4 were achieved. The resistance ratio was high enough for the high-density CBA (Mb block density), but the rectification ratio should be improved.[4] In addition, the voltage range for achieving those performances was generally too high, and as such, further engineering works are required to address these two problems. Nevertheless, the present work was devoted to the possible fabrication of an electroforming-free, highly uniform, and self-rectifying RS device structure, and to the elucidation of the underlying mechanism. **Figures 3**a and b represent the exceptionally high uniformity of the RS performances within one dot (300 μm diameter) up to 100 *I–V* sweep cycles, and within 20 dots in a single sample, respectively. The cumulative probability of the current levels of the LRS and HRS in the positive and negative bias voltage regions at particular read voltages (6, 7, and 8 V) is shown in Figure 3c, where the set and reset voltages were 12 and –8 V, respectively, and the I_{cc} was 10 μA. The distributions were extremely narrow, suggesting the exceptional uniformity of the various resistance states.

Figure 3d shows the retention data of the LRS and HRS at room temperature and at 85 °C up to 10^6 s. Both the HRS and LRS stably retained their current values (measured at 6 V) at room temperature, but the HRS current increased by about one order of magnitude after ≈10^3 s at 85 °C. The current ratio was maintained at ≈10^2, however, even after the degradation, showing the high feasibility of the present material's use as the RS element in ReRAM or CBA. The TE-area-dependent current values of the HRS and LRS read out at different voltages are shown in the inset figure in Figure 3a, where the TE area varies ≈50 times (6 500–350 000 μm^2). It is worth noting that the LRS current was almost completely independent of the TE area, suggesting that the LRS current flowed along a limited number of local spots. In contrast, the HRS current almost linearly varied according to the TE area, suggesting that the leakage current flowed uniformly across the whole TE area when the local conducting paths were removed by reset operation.

Figures 4a and b show another crucial merit of this RS system, which must be contributed by the uniform switching behavior. In Figure 4a, the variations in the HRS and LRS currents measured at 5, 6, and 7 V, respectively, are shown as a function of I_{cc} during the set switching, when the reset operation was performed by sweeping the voltage to –8 V after each set switching. The switching *I–V* curves with

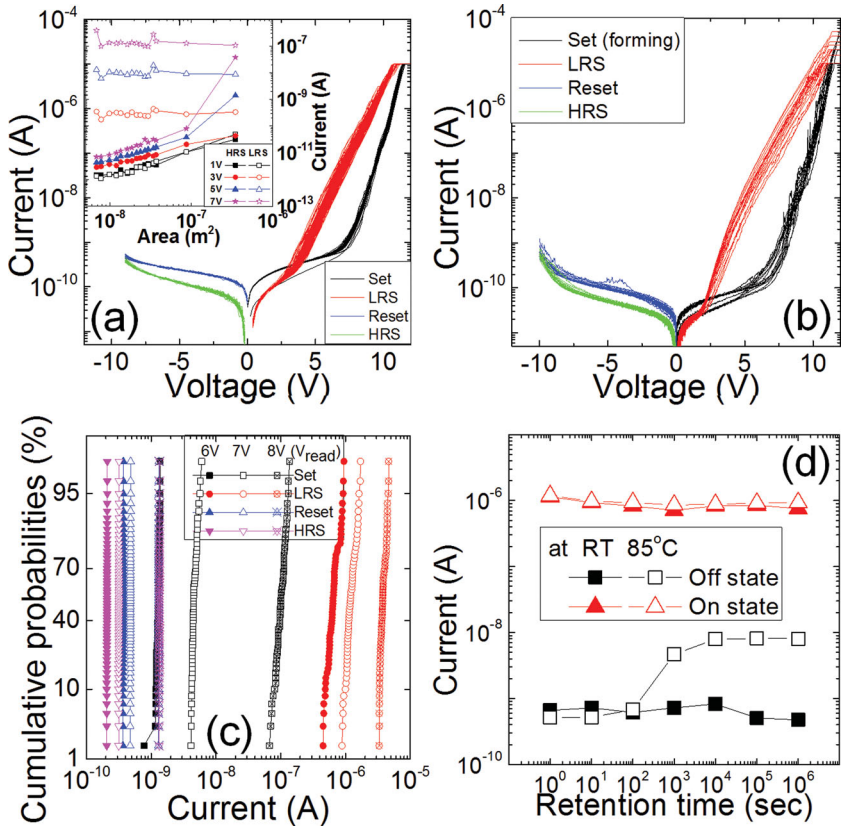

Figure 3. Exceptionally high uniformity of the RS performances within a) one dot (300 μm diameter) up to 100 *I–V* sweep cycles, and b) 20 dots in a single sample; c) cumulative probability of the current levels of LRS and HRS in the positive and negative voltage regions at particular read voltages (6, 7, and 8 V); and d) retention data of the LRS and HRS at room temperature and 85 °C up to 10^6s (measured at 6 V).

different I_{cc} values were included in Figure S3a, Supporting Information. When the I_{cc} was lower than ≈15 μA, the LRS current increased rapidly as the set switching occurred with the increasing I_{cc}. When the I_{cc} became higher than ≈20 μA, however, the LRS current was saturated at a certain value, meaning that the uncontrolled variations that might occur during set switching could be well suppressed. Figure 4b shows that the HRS current was also saturated at a certain level, even when the reset voltage decreased to sufficiently low values. The switching *I–V* curves with different reset voltages were also included in Figure S3b, Supporting Information. These two factors suggested that the switching mechanisms in this material system were not controlled by the creation and rupture of the conduction channels that could have been contributed by the drift and diffusion of the ionic defects, such as the oxygen vacancies. In the following, the possible reasons for such exceptional performance are discussed, based on the electrical-conduction mechanisms of the HRS and LRS.

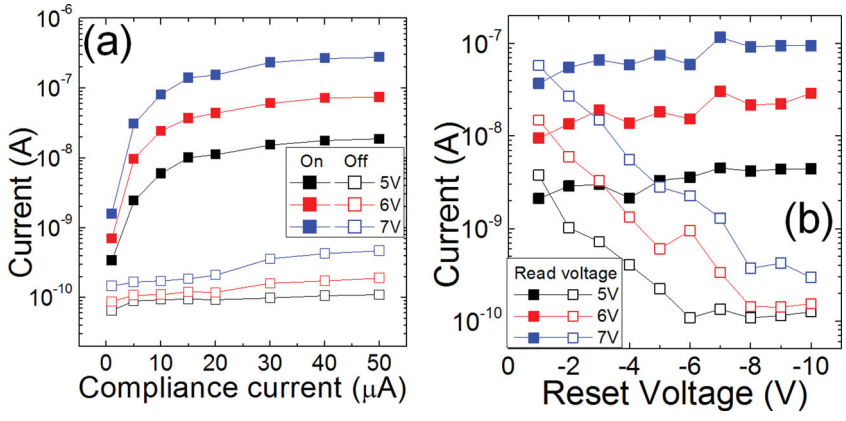

Figure 4. Variations of the current level in the HRS and LRS, measured at 5, 6, and 7 V, respectively, as a function of the a) I_{cc} during the set switching, and b) reset voltage during the reset switching.

Figure 5a shows the *I–V* curves of the LRS (dashed lines) and HRS (lines) measured at different temperatures ranging from 30 to 100 °C. Here, the HRS was attained by applying –10 V, and the LRS, by applying +12 V, with an I_{cc} of 10 μA. In both states, the current generally increased with the increasing temperature, suggesting a thermally activated mechanism. It was also evident that the voltage regions could be divided into two regions according to the current increase rate. In the low-voltage regions, both states showed a gradual increase in current, while in high-voltage regions, the current increased at a much higher rate with the voltage and temperature. For the assessment of the current conduction mechanism in the low-voltage regions, the currents at 1.0–2.5 and 1.4–2.9 V for the LRS and HRS, respectively, were plotted according to the Arrhenius form (Ln *I* vs. 1/*T*), and the activation energies (E_a) were extracted at each voltage from the best-linear-fit graphs of the data. Figure 5b shows the Ln *I* vs. 1/*T* results for HRS, and the two inset figures show the variations in the E_a for HRS and LRS. Although the plots were not shown, the log I vs. log V curves in the low-voltage region showed a slope very close to 1 for both cases. The E_a values were relatively small and were not very different for both states (0.15–0.21 eV). It is believed that the V_o values were dispersed within the HfO_2 layer and acted as the trap sites for the injected carriers in both states.[30] As the band gap of Ta_2O_5 is lower than that of HfO_2 (≈5.68 and ≈4.2 eV in HfO_2 and Ta_2O_5, respectively, estimated via Auger-electron spectroscopy reflective electron energy loss spectroscopy and spectroscopic ellipsometry, respectively), the electrons transported to Ta_2O_5 easily moved to Pt TE via the conduction within the CB of the Ta_2O_5 layer, so that the Ta_2O_5 layer did not interfere with the current conduction under the positive bias condition. The almost

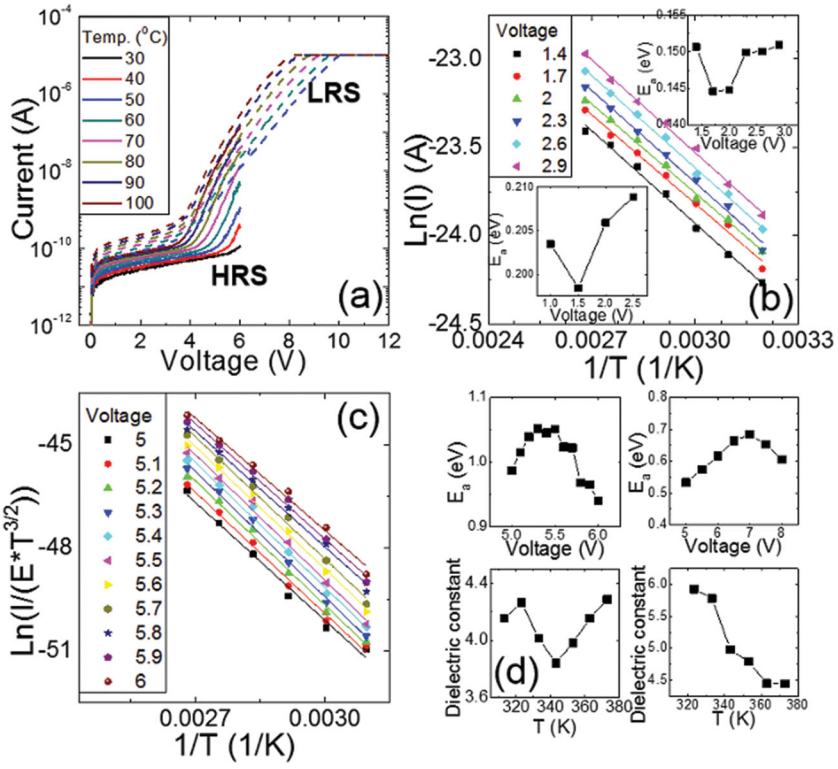

Figure 5. a) *I–V* curves of the LRS (dashed lines) and HRS (solid lines) samples measured at different temperatures ranging from 30 to 100 °C. b) Arrhenius form (Ln *I* vs. 1/*T*) plot in HRS, and (inset figures of (b)) activation energies (E_a) extracted at each voltage from the best-linear-fitting of the data in HRS and LRS. c) P–F fitting and the plots in the form of $\mathrm{Ln}(I/(E^*T^{3/2}))$ vs. 1/*T* according to the P–F equation for the voltages ranging from 5 to 6 V in HRS. (Upper panels of (d)) Activation energy, corresponding to the trap depth at each voltage in HRS and LRS (left for HRS and right for LRS), and (lower panels of (d)) dielectric constant at each temperature.

identical *I–V* curves of the pristine and HRS samples suggested that the distribution of V_o values within the HfO_2 layer did not vary during the repeated switching.

The critical differences between the currents of HRS and LRS could be found in the high-voltage region, and the *I–V* curves in the high-voltage region were attempted to be fit with the Poole–Frenkel (P–F), Schottky, and tunneling mechanisms. The best results were achieved from the P–F fitting, and the plots in the form of $\mathrm{Ln}(I/(E^*T^{3/2}))$ vs. 1/*T* according to the P–F equation for the voltages ranging from 5 to 6 V are shown in Figure 5c for the case of HRS. The results fit quite well with the P–F mechanism. Similar fitting could be made for the LRS in the voltage region (5–8 V), which also showed the suitability of the P–F conduction mechanism (data shown in Figure S4, Supporting Information). For these fittings, the electric field (*E*) was calculated by dividing the voltage applied over the HfO_2 layer, which could be estimated from the thicknesses and dielectric constants of HfO_2 (10 nm, 18) and Ta_2O_5 (10 nm, 25) and the total applied voltage, with a thickness of HfO_2, suggesting that the conduction was really governed by the HfO_2 layer. From the slopes of the best-linear-fitted graphs at each voltage, the activation energy, which corresponded to the trap depth at each voltage, could be achieved, and the results are summarized in the upper panels (left for HRS and right for LRS) of Figure 5d. The estimated trap depths for HRS and LRS were ≈1.0 and ≈0.6 eV, respectively. The accuracy of these P–F could be confirmed by the following plots of the I-V curves according to another formalism of the P–F equation: $\mathrm{Ln}(I/E)$ vs. $E^{1/2}$ graphs, which were also included in Figure S5, Supporting Information. They also showed a nice linear relationship in the high-voltage region, and from the slopes of the best-linear-fitted graphs, the dielectric constant could be estimated, which are summarized in the lower panels (left for HRS and right for LRS) of Figure 5d. While there were some variations according to the resistance states and temperatures, the estimated values of 3.8–5.9 coincided reasonably well with the optical dielectric constant of ≈3.9 calculated from the square of the refractive index (n ≈ 1.9).

When Pt TE was negatively biased, conduction mechanism analysis was similarly attempted, as shown in **Figure 6**. Under this bias condition, the current was generally low in a wider voltage range, and the activation energy obtained from the slopes of the best-linear-fitting Ln (J) vs. 1/*T* graph at voltages ranging from –1 to –5 V (data not shown) was ≈0.16 eV. The log *I*–log *V* graphs in the same voltage region showed a slope of ≈1, suggesting that the current conduction in this voltage region was also governed by the trap-assisted hopping mechanism. The almost identical E_a to the case where the TE was positively biased, estimated in Figure 5, suggests that the small leakage current was also governed by the shallow traps in HfO_2.

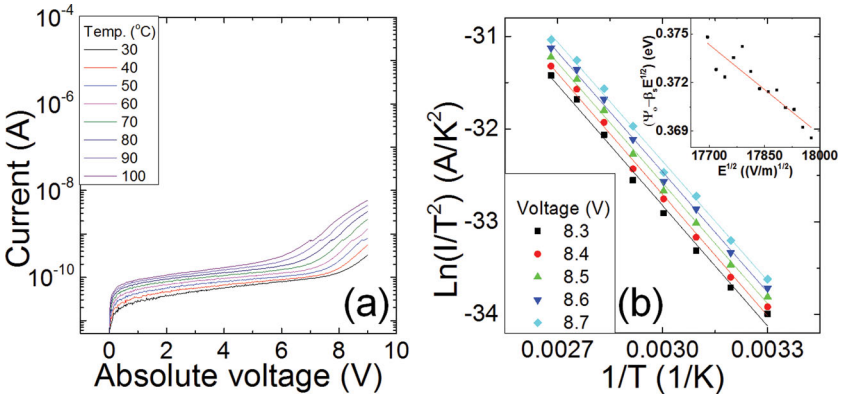

Figure 6. a) *I–V* curves under a negatively biased condition measured at different temperatures ranging from 30 to 100 °C. b) Schottky type form $\mathrm{Ln}(I/T^2)$ vs. 1/*T* plot at voltages ranging from 8.3 to 8.7 V. (Inset figure of (b)) $\psi_o - \beta_s E^{1/2}$ values plotted as a function of $E^{1/2}$.

For the lower-voltage (high-absolute-value) region, where the current increased exponentially with the voltage and temperature, the *I–V* curves in that region were plotted according to the P-F, Schottky, and tunneling equations. It was found that only the Schottky mechanism well fit the experimental data, and the $\mathrm{Ln}(I/T^2)$ was plotted vs. $1/T$ at voltages ranging from 8.3 to 8.7 V (Figure 6b). The slopes of the best-near-fit graphs corresponded to the Schottky barrier height at a given E (ψ_o–$\beta_s E^{1/2}$, where ψ_o and β_s are the zero-field Schottky barrier height and Schottky coefficient, which is determined by the optical dielectric constant). The ψ_o–$\beta_s E^{1/2}$ values were plotted as a function of $E^{1/2}$ in the inset figure in Figure 6b, the best-linear-fitting of which gave the ψ_o value of ≈0.70 eV and the dielectric constant of ≈4.2, which was close to the estimated value with the refractive index (≈2.0) of Ta_2O_5 from the ellipsometry. For this estimation, the electric field E was taken from the voltage applied over the Ta_2O_5 layer and its thickness. This estimation suggests that the low leakage current in the negative bias region was due to the suppression of the carrier injection from the Pt to the Ta_2O_5 layer by the presence of a high Schottky barrier (≈0.70 eV), which appeared to have remained intact irrespective of the resistance states in the positive bias region. This was the main reason for the achievement of a high rectification ratio. The 0.70 eV Schottky barrier does not correspond to the ideal Schottky barrier at the Pt/Ta_2O_5 interface, which could be lowered by several factors, pinning the Fermi level close to the conduction band (CB) edge.

The above estimations unveil the switching mechanism in this material system. The identification of two trap levels (0.6 and 1.0 eV) in the positive bias region suggested that these levels should be taken into account for the identification of the switching mechanism, and the electrode-area-independent LRS resistance revealed that the conduction path with the 0.6 eV of trap depth were spatially localized. This localized area might be related with several locations along the grain boundaries of the crystallized HfO_2, whereas the current path with the trap depth of 1.0 eV could be safely assumed to be the bulk HfO_2 from the electrode-area-dependent HRS resistances. The trap depth of 1.0 eV well coincided with the energy distance between the V_o from the CB edge in HfO_2.[31] Although the trap depth of 0.6 eV has not been reported in HfO_2 yet especially when the trap depth of V_o was ≈1 eV, the high Vo density and the possible interactions between them at several specific structures of grain boundaries could induce the shift of Vo level upward. (It must be noted that estimation of trap depth or additional energy location in the band gap of dielectrics generally relies upon the adopted functional in density functional theory calculations, mainly due to the band gap underestimation. Therefore, only the theoretical reports assigning the trap depth of V_o to ≈1 eV were considered in this work.) Otherwise, there could be any other defects which may form trap levels at that energy location. Another possibility for explaining the shallower trap levels could be that the energy gap of oxides near the grain boundaries are lower than the bulk,[32] so that the identical traps could induce shallower trap depth in P–F conduction. In any case, it was believed that the number of locations with such specific trap distribution must be quite limited, so that the electrode-area-independent LRS resistance could be achieved, while the electrode-area-dependent HRS resistance could be safely ascribed to the uniform (low) electrical conduction throughout the bulk portion of HfO_2.

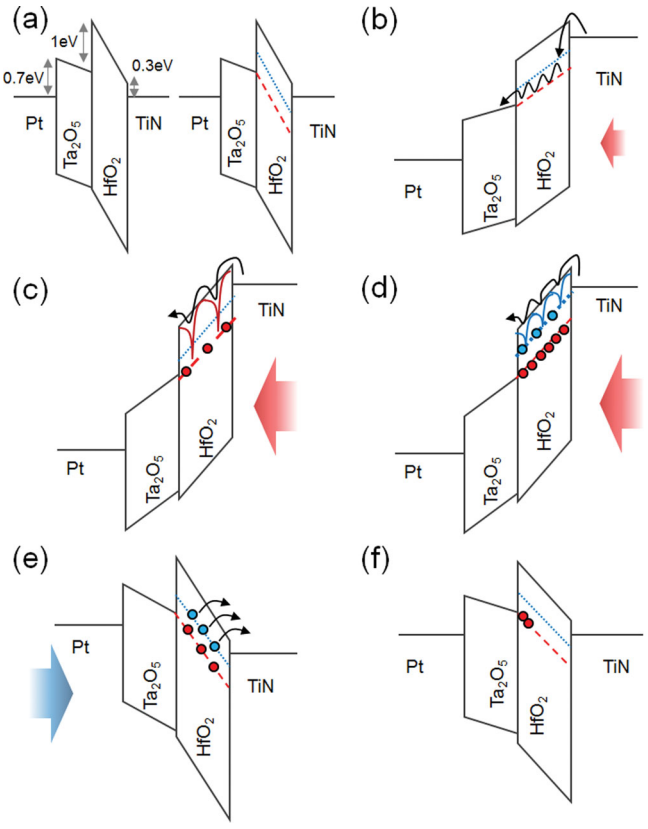

Figure 7. Schematic diagram showing the switching mechanism: a) Schematic diagrams of band structure for zero bias condition (left panel figure). The bulk of HfO_2 has the 1.0eV traps, which has coincided with the energy distance between V_o from the CB edge, while local portion of HfO_2 has the 0.6eV traps in addition to the 1.0eV traps (right panel figure). b) Under the low positive bias (≤≈3V), the injected electrons transported through the hopping mechanism. c) As the traps with 1.0 eV were filled with electrons, the P–F effect started to show up where the effective trap depth decreased at the higher positive bias. d) The carrier transport could occur via the P–F mechanism mediated by 0.6eV traps after the deeper trap level was fully filled with carriers and the system switched to LRS. e) When the low negative bias was applied to system, the electrons in the HfO_2 traps were detrapped. At the same time, carrier injection from the Pt electrode was suppressed by the Schottky barrier while the electrons from all the trap sites detrap switching back the sample to HRS. f) Even under no bias condition, some of the electrons accumulated at the Ta_2O_5/HfO_2 interface could be transported to the empty deep traps and degrade the HRS with time especially at high temperature (85 °C).

Although the accurate energy band structure could not be depicted due to the lack of precise information on the band offset between the two dielectric layers and possible (small) Schottky barrier at the HfO_2/TiN interface, a tentative schematic band diagram could be drawn as shown in **Figure 7**a for the zero external bias condition. Here, the CB offset between Ta_2O_5 and HfO_2 was taken as 1 eV considering the known electron affinities of the two materials,[33,34] and contact potential at the HfO_2/TiN interface was arbitrarily taken as 0.3 eV to make it an (quasi-) Ohmic contact. The figure in left hand panel showed the circumstance for bulk portion of HfO_2, which does not bear the specific 0.6 eV traps, and right hand panel showed

the circumstance for the local portion of HfO_2 which has the specific 0.6 eV traps in addition to the 1.0 eV traps. There must be internal bias voltage being ascribed to the different Schottky barrier heights of the two interfaces, and such internal bias must be applied over the two dielectric layers inversely proportional to their static dielectric constants. The electronic configuration of traps (trap-empty or trap-filled) could be dependent on the relative energy locations of the traps and Fermi levels of metals. However, when a small positive bias applied to the Pt TE, all the traps easily detrapped by the transport of trapped electrons to Pt TE through CB of Ta_2O_5 layer. Due to the close proximity of trap levels in HfO_2 and CB of Ta_2O_5, and always higher level of CB of HfO_2 than that of Ta_2O_5, Ta_2O_5 layer generally did not interfere with the electron transport when the electrons were injected from TiN BE through HfO_2 layer. Of course, this is not the case for negative bias condition. The initially low current and the observation of the P-F conduction mechanism with a trap depth of 1 eV suggested that the two trap levels were with the trap-empty configurations under low positive bias condition, which well coincided with the HRS. With the slight increase in the positive bias voltage to Pt TE, electrons must be injected from TiN BE to HfO_2 mainly via the thermionic emission. No observation of any tunneling-related mechanisms suggested that tunneling of electrons to trap levels from the TiN BE and trap-assisted-tunneling mechanism could be safely disregarded in this case. This must be reasonable considering the rather thick thickness of the two layers, (20 nm) and that 10 V of applied voltage coincided with average 5 MV cm^{-1}, which was generally too low to induce a significant tunneling. Under the not-so-high positive bias voltage ($\leq \approx 3$ V), the injected electrons trapped mainly at the trap levels of 1.0 eV, and transported through the hopping mechanism, as schematically shown in Figure 7b. This must be due to the low voltage which was insufficient to sufficiently decrease the trap depth by the P–F effect. It was believed that most of the traps remained empty since the degree of carrier injection must be low due to the low bias voltage. This explained the hopping mechanisms observed for both HRS and LRS shown in Figure 5b. As the voltage increased, the carrier injection became higher, and both traps started to be filled with the injected carriers. At the same time, the P-F effect started to work and the effective trap depth decreased as shown in Figure 7c. It must be noted that this effect should work for both the 0.6 and 1.0 eV depth traps, but as long as the traps with 1.0 eV were not fully filled, the operation of the 0.6 eV depth traps could not be detected since the carriers had no reason to stay in the shallower levels rather than transited to the deeper traps. This could well explain the observation of HRS current in the higher positive voltage region. When the voltage became high enough and the carrier injection overwhelmed their transport through the HfO_2 (also via Ta_2O_5) layer, the deep traps were now fully filled with carriers, and the system switched to LRS, as long as the trapped carriers did not detrap. Under this circumstance both deep and shallow traps could be filled with carriers, but the shallow traps could be detrapped temporarily under the positive bias condition due to the P–F effect, and the carrier transport could occur via the P–F mechanism mediated by the 0.6 eV traps. This could explain the observation of P-F mechanism current with 0.6 eV trap depth for the LRS.

Therefore, these mechanistic considerations suggested that the switching from the HRS to LRS under the positive bias condition corresponded to the filling of deep traps with the injected carriers, and further injected carriers transported via the local paths which contained the shallower traps. As mentioned above, these localized paths could be composed of some specific regions along the grain boundaries of HfO_2 but there was no reason why some part of bulk HfO_2 could not contribute to this local paths especially under the process conditions that the plasma-induced damage was rather serious. Such a condition could be schematically represented by the figure shown in Figure 7d. The switching back from the LRS to HRS and low current irrespective of the resistance state under the negative bias could be understood as follows.

When the bias voltage decreased to a sufficiently low negative bias, the electrons in the HfO_2 traps were detrapped while the electron injection from the Pt TE was suppressed by the high Schottky barrier height. Figure 7e showed the schematic diagram of this circumstance. This coincided with the resetting graphs in Figure 2d. Therefore, when the bias voltage was switched back to a positive direction, the drift of the electrons injected from the TiN were interfered with by the traps with a depth mainly of ≈1.0 eV, so that the current flow under this circumstance must be much lower, and HRS could be attained. This is, in fact, identical to the current conduction of the pristine state, explaining the electroforming-free property of the present sample. The degradation in the retention performance at 85 °C for the case of HRS (decrease in the HRS resistance) could be also understood from the suggested switching mechanism. When the traps became empty by the high negative bias, and bias was removed subsequently, the energy band diagram could be represented by Figure 7f. Under this circumstance, some of the electrons accumulated at the Ta_2O_5/HfO_2 layer, which were injected from the Pt electrode by thermionic emission, could be transported to the empty deep traps and degrade the HRS resistance with time (Figure 3d).

The above mentioned switching mechanism also provided a reasonable explanation for the degraded switching performances of the thinner HfO_2 film shown in Figure 2c. In this case, the total numbers of traps with both 1.0 and 0.6 eV trap depth in HfO_2 must be smaller, so that the switching performance was degraded.

The most critical feature of the above-mentioned switching mechanism is that it is related with the change in the charge state of the electron traps, presumably oxygen vacancies with different oxidation states in HfO_2, not the variations in their local spatial distribution or concentration, meaning that this is an almost purely electronic mechanism. This is closely related with the high uniformity of the memory cell. It could be noted that this type of RS mechanism had an aspect in common with the flash memory in that the electron movement for writing occurred only in one side of the devices; in the flash, electrons tunnel between the channel and the floating gate (or charge trap layer) via the tunneling oxide while their migration through the blocking oxide is strictly prohibited. In this ReRAM, during the writing operations, electrons are transported between the TiN electrode and the deep trap levels in the HfO_2 through the HfO_2 layer while their movement through the Ta_2O_5 layer is successfully suppressed by the high Schottky barrier. Of

course, the reading mechanism must be quite different in the two devices.

4. Conclusion

In this work, a feasible method of achieving a highly uniform, electroforming-free, and self-rectifying RS memory cell is presented. The method can be generally stated as having a two-layered dielectric structure, where one layer (in this case, HfO_2) works as the resistance switching layer by trapping and detrapping the deep trap sites (1.0 eV trap depth) while the other dielectric layer (in this case, Ta_2O_5) remains intact during the whole switching cycle and creates a high Schottky barrier with a high-work-function metal (in this case, Pt) to constitute the rectifying functionality. In addition, the RS layer should have a lower dielectric constant compared with the rectifying oxide layer for the effective application of the integral part of the voltage over the RS layer. In addition, the energy gap of the RS layer should be higher than that of the rectifying oxide layer to ensure that the carrier transport in the forward (or switching) bias polarity will not be disturbed by the conduction band offset between the two dielectric layers.

The present combination of the Ta_2O_5 and HfO_2 layers, which were in contact with the Pt and TiN electrode, respectively, nicely fitted the above-mentioned conditions for achieving the desired multitude of functionality from one RS system. In addition, the appropriate deoxidation effect of the PEALD process for Ta_2O_5 on the underlying HfO_2, while the deoxidation effect on Ta_2O_5 itself was minimized by the optimized process conditions, made the HfO_2 have just enough density of oxygen vacancies to induce the fluent RS within the layer. With all these optimized structure and operation conditions for the given structure, excellent RS uniformity and electroforming-free and self-rectifying functionality could be simultaneously achieved from the $Pt/Ta_2O_5/HfO_2/TiN$ structure, which could be attributed to the electronic switching mechanism, where the disturbance by the uncontrolled ion migration could be largely suppressed.

5. Experimental Section

Using an 8-inch-diameter-scale traveling-wave-type ALD reactor (CN-1 Co. Plus 200), 10-nm-thick HfO_2 films were deposited on a 50-nm-thick $TiN/SiO_2/Si$ wafer, where the TiN wafer was reactively sputter-deposited using a commercial sputtering system (Endura, Applied Materials). ALD of the HfO_2 film was performed using $Hf[N(CH_3)(C_2H_5)]_4$ and O_3 as the Hf precursor and oxygen source, respectively. The Hf precursor and O_3 pulse durations were 2 and 3 s, respectively, and Ar purge gas was injected for 9 and 3 s, respectively, after the occurrence of each of these two chemical pulses. The wafer temperature during the deposition was set to 280 °C. The PEALD Ta_2O_5 layer was deposited in another shower-head-type ALD reactor using tert-butylimido-bis(diethylamido) cyclopentadienyl)tantalum and H_2O-activated plasma (300 W) as the Ta precursor and oxygen source, respectively, at a substrate temperature of 200 °C. The PEALD Ta_2O_5 sequence consisted of Ta precursor feeding (5 s), Ar purging (7 s), water vapor pulsing (5 s, plasma power was turned on during the last 4 s), and Ar purging (10 s).

The film thickness, depth profile of each element, and chemical status of the films were examined using an ellipsometer (Gaertner Scientific Corporation, L116 D), AES (Perkin-Elmer, PHI 660), and XPS (ThermoVG, Sigma Probe), respectively. The cross-section of the $Pt/Ta_2O_5/HfO_2/TiN$ sample was observed using a high-resolution TEM (JEOL, JEM-3000F). For electrical measurement, Pt top electrodes were electron-evaporated through a 300-μm-hole-diameter metal shadow mask and the lift-off process for fabricating samples with different electrode areas (6 500–350 000 μm^2). The self-rectifying resistive switching behavior was measured using an HP4145B semiconductor parameter analyzer at room temperature, in voltage sweep mode. Each voltage sweep began from 0 V, and the bias was applied to the TE while the BE was grounded.

Supporting Information

Supporting information is available from Wiley Online Library or from the author.

Acknowledgements

This study was supported by the Converging Research Center Program through a National Research Foundation of Korea (NRF) grant funded by the Ministry of Education, Science, and Technology of the Republic of Korea (2013K000158), and by the Global Research Laboratory Program (2012040157), also through an NRF grant.

Received: January 8, 2014
Revised: February 26, 2014
Published online: May 26, 2014

[1] J. Borghetti, G. S. Snider, P. J. Kuekes, J. J. Yang, D. R. Stewart, R. S. Williams, *Nature* **2010**, *464*, 873.
[2] E. Linn, R. Rosezin, C. Kugeler, R. Waser, *Nat. Mater.* **2010**, *9*, 403.
[3] S. H. Jo, K. Kim, W. Lu, *Nano Letters* **2009**, *9*, 870.
[4] G. H. Kim, J. H. Lee, Y. Ahn, W. Jeon, S. J. Song, J. Y. Seok, J. H. Yoon, K. J. Yoon, T. J. Park, C. S. Hwang, *Adv. Funct. Mater.* **2012**, *23*, 1440.
[5] M. J. Lee, C. B. Lee, D. Lee, S. R. Lee, M. Chang, J. H. Hur, Y. Kim, C. Kim, D. H. Seo, S. Seo, U. Chang, I. Yoo, K. Kim, *Nat. Mater.* **2011**, *10*, 625.
[6] J. Y. Seok, S. J. Song, J. H. Yoon, K. J. Yoon, T. H. Park, D. E. Kwon, H. Lim, G. H. Kim, D. S. Jeong, C. S. Hwang, submitted to *Adv. Funct. Mater.*
[7] D. Kwon, K. M. Kim, J. H. Jang, J. M. Jeon, M. H. Lee, G. H. Kim, X. Li, G. Park, B. Lee, S. Han, M. Kim, C. S. Hwang, *Nat. Nanotechnol.* **2010**, *5*, 148.
[8] B. J. Choi, D. S. Jeong, S. K. Kim, C. Rohde, S. Choi, J. H. Oh, H. J. Kim, C. S. Hwang, K. Szot, R. Waser, B. Reichenberg, S. Tiedke, *J. Appl. Phys.* **2005**, *98*, 033715.
[9] G. Park, X. Li, D. Kim, R. Jung, M. Lee, S. Seo, *Appl. Phys. Lett.* **2007**, *91*, 222103.
[10] K. M. Kim, B. J. Choi, C. S. Hwang, *Nanotechnology* **2011**, *22*, 254002.
[11] K. M. Kim, B. J. Choi, C. S. Hwang, *Appl. Phys. lett.* **2007**, *90*, 242906.
[12] S. J. Song, J. Y. Seok, J. H. Yoon, K. M. Kim, G. H. Kim, M. H. Lee, C. S. Hwang, *Sci. Rep.* **2013**, DOI: 10.1038/srep03443.
[13] N. Huby, G. Tallarida, M. Kutrzeba, S. Ferrari, E. Guziewicz, Ł. Wachnicki, M. Godlewski, *Microelectron. Eng.* **2008**, *85*, 2442.
[14] G. H. Kim, J. H. Lee, J. H. Hwan, S. J. Song, J. Y. Seok, J. H. Yoon, K. J. Yoon, M. H. Lee, T. J. Park, C. S. Hwang, *Appl. Phys. Lett.* **2012**, *100*, 213508.

[15] W. Y. Park, G. H. Kim, J. Y. Seok, K. M. Kim, S. J. Song, M. H. Lee, C. S. Hwang, *Nanotechnology* **2010**, *21*, 195201.
[16] J. Huang, Y. Tseng, C. Hsu, T. Hou, *IEEE Electron Device Letters* **2011**, *32*, 1427.
[17] W. Lee, J. Park, S. Kim, J. Woo, J. Shin, G. Choi, S. Park, D. Lee, E. Cha, B. h. Lee, H. Hwang, *ACS NANO* **2012**, *6*, 8166.
[18] M. Son, J. Lee, J. Park, J. Shin, G. Choi, S. Jung, W. Lee, S. Kim, S. Park, H. Hwang, *IEEE Electron Device Letters* **2011**, *32*, 1579.
[19] G. D. Wilk, R. M. Wallace, J. M. Anthony, *J. Appl. Phys.* **2001**, *89*, 5243.
[20] B. Govoreanu, G. S. Kar, Y.-Y. Chen, V. Paraschiv, S. Kubsek, A. Fantini, I. P. Radu, L. Goux, S. Clima, R. Degraeve, N. Jossart, O. Richard, T. Vandeweyer, K. Seo, P. Hendrix, G. Pourtois, H. Bender, L. Altimine, D. J. Wouters, J. A. Kittl, M. Jurczak, *IEDM Tech. Dig.* **2011**, 729.
[21] P. Gonon, M. Mougenot, C. Vallee, C. Jorel, V. Jousseaume, H. Grampeix, F. El Kamel, *J. Appl. Phys.* **2010**, *107*, 074507.
[22] J. H. Hur, M. Lee, C. B. Lee, Y. Kim, C Kim, *Phys. Rev. B* **2010**, *82*, 155321.
[23] C. Y. Dong, L. Shi, D. S. Shang, W. Chen, J. Wang, B. G. Shen, J. R. Sun, *J. Phys. D: Appl. Phys.* **2011**, *44*, 205302.
[24] K. M. Kim, B. J. Choi, M. H. Lee, G. H. Kim, S. J. Song, J. Y. Seok, J. H. Yoon, S. Han, C. S. Hwang, *Nanotechnology* **2011**, *22*, 254010.
[25] K. M. Kim, G. H. Kim, S. J. Song, J. Y. Seok, M. H. Lee, J. H. Yoon, C. S. Hwang, *Nanotechnology* **2010**, *21*, 305203.
[26] K. J. Yoon, S. J. Song, J. Y. Seok, J. H. Yoon, G. H. Kim, J. H. Lee, C. S. Hwang, *Nanotechnology* **2013**, *24*, 145201.
[27] S. F. Ho, S. Contarini, J. W. Rabalais, *J. Phys. Chem.* **1987**, *91*, 4779
[28] J. Lim, B. Oh, W. Lee, K. Lee, H. Na, B. Kim, D. Seo, J. Han, J. Hwang, *Appl. Phys. Lett.* **2009**, *95*, 123503.
[29] B. Vincent Crist, *Handbook of Monochromatic XPS Spectra*, John Wiley & Sons, Oxford, UK, **2000**.
[30] P. Broqvist, A. Pasquarello, *Appl. Phys. Lett.* **2006**, *89*, 262904.
[31] J. L. Gavartin, D. Munoz Ramo, A. L. Shluger, G. Bersuker, B. H. Lee, *Appl. Phys. Lett.* **2006**, *89*, 082908.
[32] K. P. McKenna, A. L. Shluger, *Proc. R. Soc. A* **2011**, *467*, 2043.
[33] W. Zheng, K. H. Bowen, J. Li, I. Dabkowska, M. Gutowski, *J. Phys. Chem. A* **2005**, *109*, 11521.
[34] B. C. Lai, N. Kung, J. Y. Lee, *J. Appl. Phys.* **1999**, *85*, 4087.